






Cite this: *J. Mater. Chem. A*, 2019, 7, 24477

A functional-gradient-structured ultrahigh modulus solid polymer electrolyte for all-solid-state lithium metal batteries†

Jie Liu,  Jinqiu Zhou,  Mengfan Wang,  Chaoqun Niu, Tao Qian * and Chenglin Yan *

There is a contradiction between achieving a high modulus solid polymer electrolyte (SPE) and good interface contact in all-solid-state lithium metal batteries to prohibit the dendrite growth and increase the cell cyclability, respectively. Herein, we report a new functional-gradient-structured ultrahigh modulus SPE (FG-SPE) by integrating a ceramic-rich phase and polymer-rich phase. The ceramic-rich phase physically prohibits the dendrite growth, while the polymer-rich phase improves the interface compatibility between the cathode and electrolyte. As a result, this ultrahigh modulus solid polymer electrolyte renders a low charging voltage polarization of 0.5 mA h cm⁻² for FG-SPE-based symmetrical batteries. All-solid-state Li/LiFePO₄ batteries based on this material show a high specific capacity of 163.2 mA h g⁻¹ at 0.1C, and a high reversible capacity could still be obtained even at a rate of 2C. Importantly, the active material could achieve a high mass loading of 15.6 mg cm⁻², which is significant for practical applications.

Received 20th July 2019
Accepted 23rd September 2019

DOI: 10.1039/c9ta07876b

rsc.li/materials-a

Introduction

Compared to commercially used graphite anodes, lithium metal anodes possess many attractive advantages, such as the highest capacity (3860 mA h g⁻¹) and the lowest potential (-3.040 V *versus* a standard hydrogen electrode), which make lithium metal batteries (LMBs) a popular research field for energy storage systems with a higher energy density.¹⁻⁴ However, the current LMBs derived from liquid electrolytes always suffer from several problems, including an unstable solid-electrolyte interphase, poor cycling performance, flammability, dendrite growth, and leakages, causing a potential safety hazard in vehicle and grid applications.⁵⁻⁷ Solid-state LMBs provide a promising approach to address these primary problems in liquid LMB systems, and so solid-state electrolytes have attracted significant attention from both the academic and industrial communities.^{8,9} In general, solid-state electrolytes fall into two categories: inorganic solid electrolytes and solid polymer electrolytes (SPEs).¹⁰ Although advanced inorganic solid electrolytes can achieve high ionic conductivities at ambient temperature (~10⁻³ S cm⁻¹), some obstacles severely impede their development, basically their poor interfacial contact and

inflexibility, which lead to a high interphase-contact resistance.¹¹⁻¹³ SPEs have a macromolecular architecture, in which lithium salts are dissolved.¹⁴ One of the competitive advantages of SPEs compared with inorganic solid electrolytes is their compatible interfacial contact, making SPEs an important aid to the process of high energy density solid-state LMBs developments.^{9,15,16}

Currently, Li dendrite growth is almost unavoidable, and is related to various factors, including the nucleation location, the quality of solid electrolyte interphase, electronic field, and diffusion flux, as well as other external conditions, such as the charging current density, charging capacity, operating temperature, and inner pressure of the LMB.¹⁷⁻²⁰ Although many suppression methods of dendrites are continuously proposed, they are faced with various kinds of difficulties and problems in stabilizing batteries, like complicated processing, short-term stability, incompatibility with other components, and how they act in specific systems.^{18,19} It has been documented that non-uniform Li deposition can be completely arrested when the modulus of the separator is 1.8 times that of lithium metal.^{21,22} This condition is met for a modulus $G \sim 6.0$ GPa at room temperature.²¹ Although SPEs have great advantages in fabrication, they are typically mechanically too weak to effectively prohibit the growth and extension of Li dendrites. Traditional composite polymer electrolytes with ceramic fillers often enhance the amorphous region of the polymer and thus improve the ionic conductivity of SPEs, but the mechanical strength cannot be well improved.^{9,14,23} When a small amount of ceramic nanoparticles are filled in, the composite SPEs cannot

Soochow Institute for Energy and Materials Innovations, College of Energy, Key Laboratory of Advanced Carbon Materials and Wearable Energy Technologies of Jiangsu Province, Soochow University, Suzhou 215006, China. E-mail: tqian@suda.edu.cn; c.yan@suda.edu.cn

† Electronic supplementary information (ESI) available. See DOI: 10.1039/c9ta07876b

form a compact structure and afford the interconnected reinforcement to resist the dendrite growth, allowing the dendrites to eventually penetrate the solid electrolyte after several charging/discharging cycles. On the other hand, plenty of inorganic fillers lead to the agglomeration of ceramic particles and thus a lack of continuity of the high modulus domain, which would be an obstruction for their mixing with polymers to fabricate uniform SPEs on a large scale and lead to favoring the growth of Li dendrites in the low-modulus region.^{24,25} Moreover, achieving a high modulus of SPEs and good interface contact seems to involve contradictory objectives, and hence achieving both at the same time represents a puzzle for the development and operation of high energy and stable solid-state LMBs.

Functional gradient materials, which are composed of two or more materials with continuous gradient changes in composition, structure, and properties, have been widely used in the materials community.^{26–28} The gradients can be designed at the microstructural level to customize materials for certain functions or performance requirements, which are supposed to allow an optimum combination of component properties.^{27,28} Some electrolytes were reported with a concentration gradient, electric, or chemical potential gradient, or temperature gradient to complete a single achievement for a high Li⁺ flux, suppressing dendrite growth or improving the ionic conductivity of the electrolyte, *etc.*^{29–32} To date, there have been no reports of gradient composite electrolytes focused on the interface connection between the electrolyte and electrode, which is always a key issue in solid-state batteries, let alone cooperative solutions to solve the fundamental problems of solid-state batteries, such as Li dendrite growth, conductivity, or interface resistance.

Herein, we designed a functional gradient SPE (FG-SPE) composed of a ceramic-rich phase and polymer-rich phase with continuous ceramic domains. The *in situ* polymerized solid polymer frameworks accommodate the gaps between ceramic particles, sufficiently restraining their agglomeration, and also provide a compatible connection between the electrodes and solid electrolyte. Differing from the reported gradient electrolytes with a single function, the FG-SPE achieved combined functions to satisfy the cathode and anode thanks to the ceramic-rich phase and polymer-rich phase. The compact ceramic-rich phase not only had a high modulus and served as a physical barrier to dendrite growth, but also displayed depolarization effects on the Li/electrolyte interface, thereby avoiding uneven lithium deposition (Fig. 1). The measured modulus of the ceramic-rich phase increased to 6.67 GPa, much higher than the control SPE (~0.25 GPa), which indicates its effectiveness to prohibit the penetration of Li dendrites. In the meanwhile, the polymer-rich phase with a moderate modulus, filled in with a small amount of ceramics, improved the cathode/electrolyte interface compatibility and the conductivity of the polymer, which was conducive to vastly enhancing the cathode mass loading. Owing to this smart functional gradient structure, the FG-SPE demonstrated excellent electrode/electrolyte interfacial stability and cyclability in fabricated all-solid-state Li batteries. The Li/FG-SPE/Li symmetrical cells

exhibited ultrastable plating/stripping behaviors with a low charging voltage polarization of ~30 mV over 1200 h at the current density of 0.1 mA cm⁻² for 0.1 mA h cm⁻². Also the stable Li plating/stripping process could be achieved even at 0.5 mA cm⁻² for 0.5 mA h cm⁻². In addition, by combining SPE with a lithium iron phosphate (LiFePO₄, LFP) cathode and Li anode, a specific capacity of 163.2 mA h g⁻¹ was obtained at 0.1C rate (1C = 170 mA g⁻¹) at room temperature and the battery's cycle life could be extended to 500 cycles at 1C rate. Importantly, the active material could achieve a high mass loading of 15.6 mg cm⁻², which is significant for practical application.

Results and discussion

A mixture of diallyl carbonate (DAC)/vinylene carbonate (VC) containing inorganic ceramic particles (Li₁₀GeP₂S₁₂, LGPS) was used as the precursor of FG-SPE. Subsequently, the precursor solution was uniformly incorporated into a cellulose separator, which was used as the mechanical support for the polymer electrolyte, and then an *in situ* polymerization process was conducted to yield a compact and robust ceramic-rich phase on the surface of the Li anode, as well as to form a moderate and compatible connection between the cathode and electrolyte. The detailed process is presented in the experimental section. A DAC/VC mixture, without the addition of LGPS nanoparticles, was prepared as a comparison after polymerization on a cellulose separator (PDVC-SPE). From the Fourier transform infrared spectroscopy (FTIR) analysis, it was seen that the transmittance peak at 3170 cm⁻¹ vanished and a new peak appeared at ~2982 cm⁻¹ after polymerization, which was attributed to the structure transition from a =C–H bond to –C–H bond (Fig. 2a). The weakened peak at 1635 cm⁻¹, corresponding to the stretching vibrations of C=C bond, clearly demonstrated the successful polymerization.^{33,34} The chemical compatibility between LGPS and DAC/VC was confirmed by X-ray diffraction (XRD). After immersing LGPS in the DAC/VC mixture for 24 h, the powder was used for XRD analysis. As shown in Fig. S1,† almost the same XRD patterns of the pristine LGPS and the LGPS in the DAC/VC mixture were obtained, indicating that LGPS and DAC/VC were chemically compatible.³⁵ Moreover, the XRD pattern of LGPS in PDVC, which was obtained by polymerizing the DAC/VC mixture containing LGPS powder, was also investigated and no new peak was observed in contrast to the pattern of pristine LGPS, indicating the stability of LGPS during the *in situ* polymerization.^{35,36} The typical images before and after the polymerization of DAC/VC with and without the LGPS additives are shown in Fig. S2.† After being *in situ* polymerized on the Li anode, scanning electron microscopy (SEM) was used to observe the cross-sectional images of PDVC-SPE and FG-SPE, as shown in Fig. 2b and c, which exhibited that the solid polymer was uniformly covered on the Li metal. The functional gradient structure of SPE was composed of a ceramic-rich phase and polymer-rich phase, as shown in the cross-sectional image of FG-SPE (Fig. 2c and S3†). The enlarged cross-sectional SEM image and elemental mapping of FG-SPE in Fig. S3† clearly display the gradient structure and the gradient

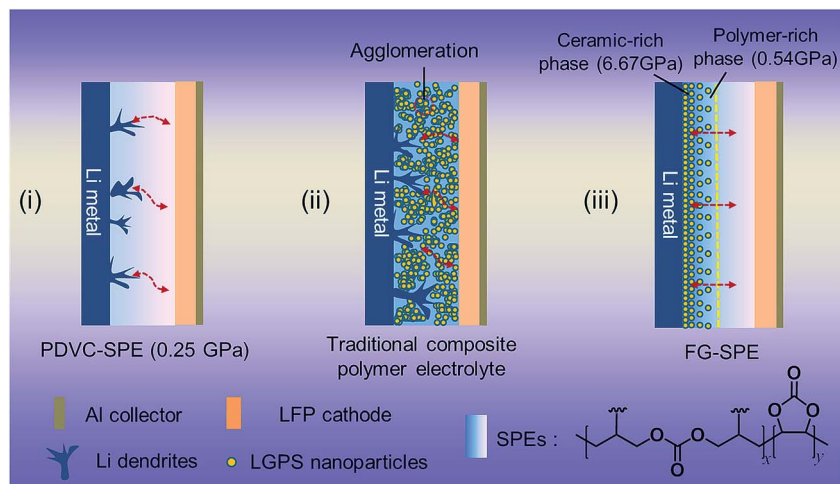


Fig. 1 Schematic demonstrating the working principle of the lithium metal anode based on different solid polymer electrolytes: (i) in the PDVC-SPE-based Li/LFP battery, the Li dendrites can easily grow and penetrate through the electrolyte due to the poor mechanical strength; (ii) the traditional composite polymer electrolyte cannot form a compact structure, leading to the lack of continuity of the high modulus domain, which induces the dendrite growth in the low-modulus region; (iii) in the FG-SPE-based cell, the ceramic-rich phase acts as a physical barrier to lithium dendrite growth due to its high modulus, and the polymer-rich phase improves the cathode/electrolyte interface compatibility and the conductivity of polymer, which is conducive to vastly enhancing the cathode mass loading.

distribution of the C, O, Ge, P, and S elements. Through *in situ* polymerization, the electrode/electrolyte interface compatibility could also be improved. In addition, we also investigated the structures of FG-SPEs that were *in situ* polymerized in different cells, including Li/Li symmetric cell, Li/stainless steel (SS) cell, and Li/LFP cell, and the cross-sectional SEM results revealed that the different interfaces had no impact on the functional gradient structure of FG-SPEs (Fig. S4a–f†).

It is known that a high modulus of the polymer can sufficiently prevent Li dendrite propagation.^{21,37} Herein, atomic force microscopy (AFM) was conducted to study the mechanical properties of PDVC-SPE and FG-SPE. Fig. 2d displays the schematic for the AFM. The cantilever is deflected when the tip is loaded/unloaded at the sample surface, and a change in signal occurs and is studied. The force–deformation curves of different samples are exhibited in Fig. 2e, f, and S5.† Both the ceramic-

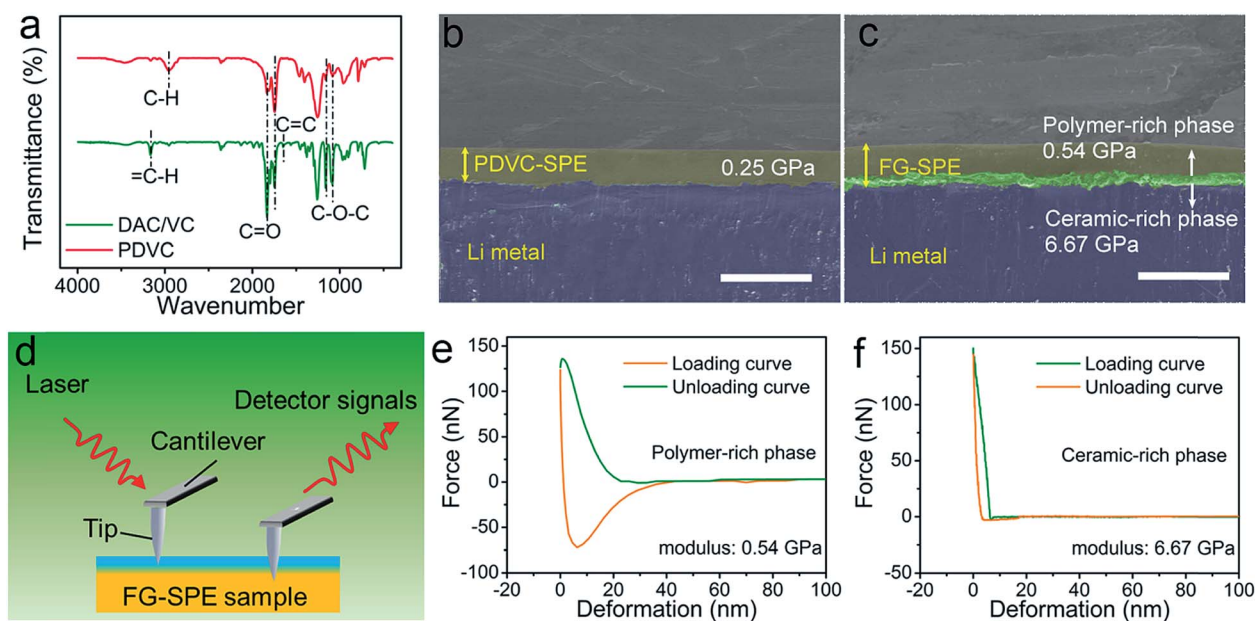


Fig. 2 Characterization of the PDVC-SPE and FG-SPE: (a) FTIR spectra comparison of the DAC/VC mixture before and after polymerization. The chemical structure change of $=\text{C}-\text{H}$ bond into $\text{C}-\text{H}$ bond and the weakened peaks of $\text{C}=\text{C}$ double bond clearly demonstrate the successful polymerization. The cross-sectional SEM images of: (b) PDVC-SPE and (c) FG-SPE polymerized on Li metal, displaying the ceramic-rich phase and polymer-rich phase. Scale bars 50 μm . (d) Schematic of the AFM investigation. Indentation curves of the: (e) polymer-rich phase and (f) ceramic-rich phase of FG-SPE.

rich phase and the polymer-rich phase have higher moduli than PDVC-SPE (0.25 GPa), implying that the FG-SPE is stiff. The ultrahigh modulus of the ceramic-rich phase (6.67 GPa) contributes to resisting the mechanical deformation resulting from Li plating/stripping and helps to prohibit dendrite growth, while the moderate modulus of the polymer-rich phase (0.54 GPa) contributes to a better connection between the cathode and electrolyte, which is quite significant for improving the cathode mass loading. Fig. S6a and b† show the topographic images of PDVC-SPE and FG-SPE, respectively, demonstrating that FG-SPE had a smooth topography with many particulates uniformly covering it.

To visually demonstrate FG-SPE's suppression of dendrite growth, we further observed the Li plating/stripping process in a well-designed sealed transparent cell, as recorded using an optical microscope. The liquid DAC/VC electrolyte with LGPS additive was polymerized on the Li foils in advance. Subsequently, Li foil covered with FG-SPE was employed as the working electrode and bare Li foil was used as the counter electrode. The cell was assembled using EC/DEC as an electrolyte to simulate the process of Li dendrite propagation in the solid-state LMB system. The control experiments were carried out using the same process except for using PDVC-covered Li foil and bare Li foil as the working and counter electrodes, respectively. Next, 4.0 mA cm^{-2} of current was applied to the electrode so that the Li deposition conducted on the working electrode and obvious Li plating behavior could be observed. Fig. 3a–c show the optical microscopy images of the different Li anodes taken at different times of Li deposition, which were all captured from videotaping the process, as shown in Movies 1, 2, and 3, respectively, in the ESI.† Before cycling (0 min), the surfaces of the electrodes were all smooth. However, for the bare Li electrode, dendritic Li generated in 1 min (Fig. 3a). The uneven deposition resulted in the licentious growth of dendrites and pulverization, and then moss quickly spread on the bare Li surface. Although no dendrite could be observed at

the early stage of Li plating (0–3 min) for the PDVC-covered Li electrode, uneven Li deposition happened and protrusions started to penetrate the PDVC layer after ~ 3 min of Li plating, which indicated that the PDVC-SPE could not resist the dendrites for a long time (Fig. 3b). In contrast, during 15 min of Li deposition, the Li foil covered with FG-SPE always kept a smooth morphology without dendrite formation (Fig. 3c). This visually strong comparison convinced us that FG-SPE had the capability to suppress dendrite growth for a long time.

The critical current density was examined in a Li/FG-SPE/Li symmetrical cell using direct current cycling, which is admitted as the lowest current density at which a battery short can occur because of metallic Li penetration. As shown in Fig. S7,† the critical current density was determined to be 0.6 mA cm^{-2} when stepping the current density from 0.1 to 1.0 mA cm^{-2} . In order to evaluate the effect of FG-SPE on resisting lithium dendrite growth in batteries and to study the efficacy for improving electrochemical performances, Li/FG-SPE/Li symmetrical cells were assembled and tested. PDVC-SPE was used as a contrast in the control symmetrical cell. Fig. 4a shows the voltage profile of Li symmetrical cells based on FG-SPE and PDVC-SPE at 0.1 mA cm^{-2} with a capacity of 0.1 mA h cm^{-2} . The Li/PDVC-SPE/Li symmetrical cell demonstrated a relatively stable voltage plateau that lasted for 150 h during the early charge/discharge process. However, conspicuous voltage fluctuation could be observed and a sudden voltage drop happened in 280 h, which was attributed to the “dynamic short-circuit,” illustrating that the PDVC-SPE had been penetrated in the prolonged cycle.^{38,39} In contrast, for the Li/FG-SPE/Li symmetrical cell, no short-circuit indication was detected during 1200 h of plating/stripping and the voltage profile still remained stable at $\sim 30 \text{ mV}$, illustrating that the stability was a result of good mechanical promotion and good ion diffusion. A similar phenomenon could be seen at 0.2 mA cm^{-2} with a capacity of 0.2 mA h cm^{-2} (Fig. 4b). The Li/FG-SPE/Li symmetrical cell always maintained a stable voltage plateau for 500 h of Li

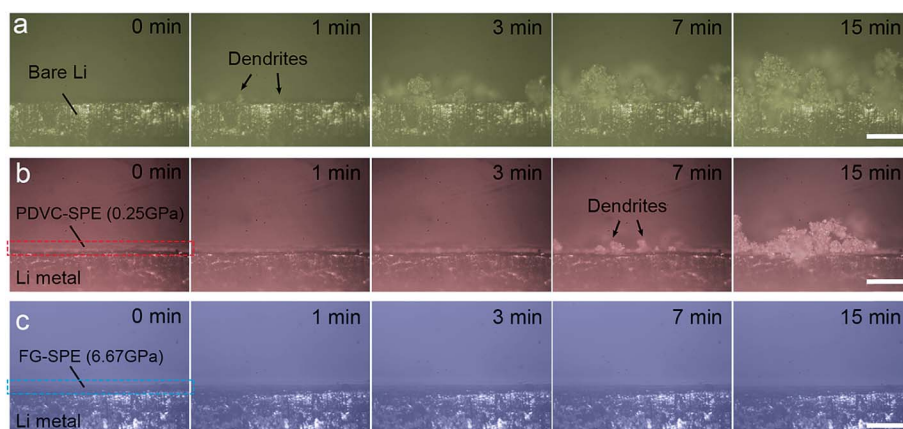


Fig. 3 Optical microscopy study of Li deposition. *In situ* optical microscopy observations of the lithium deposition process on: (a) bare Li foil, (b) PDVC-SPE-covered Li foil and (c) FG-SPE-covered Li foil at 4 mA cm^{-2} . To simulate the process of Li dendrite propagation in a solid-state LMB system, PDVC-SPE and FG-SPE were pre-polymerized on the surface of bare Li foils and then were assembled in a symmetrical transparent cell using EC/DEC as the electrolyte. The deposition processes were recorded at different plating/stripping times. All the scale bars were the same (100 μm).

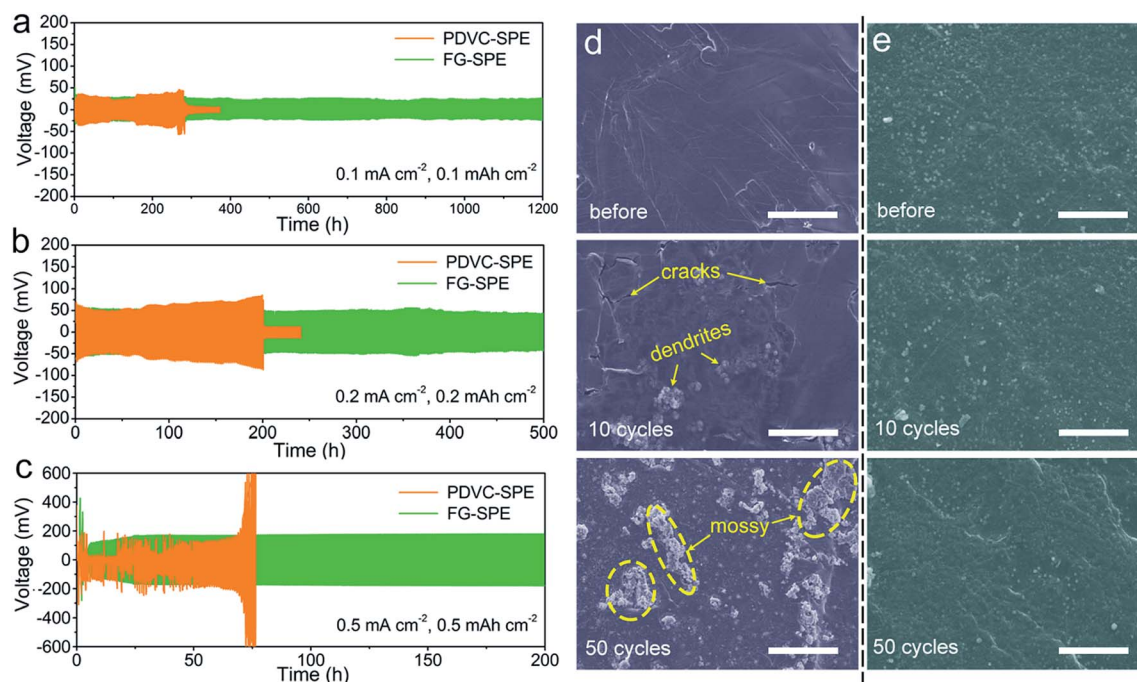


Fig. 4 Electrochemical properties of Li/PDVC-SPE/Li and Li/FG-SPE/Li symmetrical cells and the morphology changes of Li foils after cycling. Chronopotentiometry results of symmetrical cells at room temperature at the current density of: (a) 0.1 mA cm^{-2} , (b) 0.2 mA cm^{-2} , and (c) 0.5 mA cm^{-2} for 1 h, respectively. The surface SEM images of Li foil electrodes disassembling from: (d) Li/PDVC-SPE/Li and (e) Li/FG-SPE/Li symmetrical cells, respectively, before, after 10 times and 50 times of Li stripping/plating. The current density was maintained at 0.5 mA cm^{-2} with a stripping/plating capacity of 0.5 mA h cm^{-2} . Scale bars $20 \mu\text{m}$.

deposition, while the overpotential of the Li/PDVC-SPE/Li symmetrical cell constantly increased till a short-circuit happened at 200 h. The further cycling stability is shown in Fig. 4c, with an increased current density of 0.5 mA cm^{-2} and higher plating/stripping capacity of 0.5 mA h cm^{-2} . An irregular and fluctuating voltage was quickly noticed in the Li/PDVC-SPE/Li symmetrical cell, while stable cycling was attained for more than 200 h in the Li/FG-SPE/Li symmetrical cell, evidencing that the FG-SPE could achieve a higher capacity without sacrificing the cycle stability. In addition, the stable Li plating/stripping behavior at high capacity was important to evaluate the SPE's resistance to dendrite growth. Next, a 3 h Li plating and 3 h stripping routine were further conducted at current densities of 0.1 mA cm^{-2} and 0.2 mA cm^{-2} . As exhibited in Fig. S8,† the overpotentials dramatically increased and a voltage drop was quickly observed in the Li/PDVC-SPE/Li symmetrical cell, indicating the cell failure resulting from a dendrite-induced short-circuit. The cells collapsed much more rapidly when the current density was increased to 0.2 mA cm^{-2} , as shown in Fig. S9.† On the contrary, the Li/FG-SPE/Li symmetrical cell could always keep stable at the corresponding plating/stripping current densities and capacities, suggesting a stable and sufficient dendrite growth suppression by FG-SPE. These results demonstrated that the cycling stability of Li/FG-SPE/Li cells outperformed that of Li/PDVC-SPE/Li symmetrical cells, with a consistently lower polarization voltage and more stable plateaus, which indicated that FG-SPE had much better stability against dendritic lithium because the ceramic-rich phase acted as an effective physical barrier to restrict the dendrite growth.

To further demonstrate the effectiveness of the ceramic-rich layer for suppressing dendrite penetration, Li/ceramic-rich + polymer-rich + ceramic-rich/Li symmetrical cells with two sides of ceramic-rich layers were assembled and tested at 0.2 mA cm^{-2} and 0.5 mA cm^{-2} with fixed capacities of 0.2 mA cm^{-2} and 0.5 mA cm^{-2} , respectively. As expected, the cells displayed higher stability than that of the Li/FG-SPE/Li symmetrical cell (one side with a ceramic-rich layer), as shown in Fig. S10 and S11,† which indicated that having two sides with a ceramic-rich layer could extend the lifespan of symmetrical cells due to their more powerful suppression of dendrite penetration.

EIS measurements of Li symmetrical cells based on PDVC-SPE and FG-SPE were carried out and the results before and after Li plating/stripping are exhibited in Fig. S12a and b.† Both Li/PDVC-SPE/Li and Li/FG-SPE/Li symmetrical cells had a relatively low interfacial impedance before cycling, as estimated from the semicircle in the high-frequency range. However, over 50 times performing the Li plating/stripping process, the Li/PDVC-SPE/Li cell presented an obviously ever-increasing trend in interfacial impedance, which demonstrated that the continual plating/stripping behavior deteriorated the Li/electrolyte interface. In contrast, for the Li/FG-SPE/Li symmetrical cell, the interfacial impedance always remained at a low level, revealing a close and stable interface between the Li electrode and electrolyte. After plating/stripping at 0.5 mA cm^{-2} , the morphology variations of Li anodes in the different symmetrical cells were recorded and the results are presented in Fig. 4d and e. When PDVC-SPE was employed in Li symmetrical cells, the Li foil exhibited a generally smooth morphology before plating (Fig. 4d). However, the Li

surface began to become rough and uneven after 10 times of plating/stripping. Eventually, after 50 cycles of Li deposition, plentiful mossy and rugged Li covered the Li surface, which was attributed to the limited inhibition of PDVC-SPE to excessive Li dendrites. Fig. 4e exhibits the Li surface in FG-SPE-based symmetrical cells before and after cycling, and it can be seen that the top surface was maintained as flat and smooth without detectable Li dendrites.

A wide and stable electrochemical window is quite significant for high-performance solid-state LMBs.^{33,40} A Li/FG-SPE/SS asymmetrical cell was assembled to evaluate the stable voltage window of FG-SPE. As can be seen from the linear sweep voltammetry (LSV) in Fig. 5a, the SPE was stable up to 5.3 V *versus* Li/Li⁺. Besides, high ionic conductivity at ambient temperature is another important parameter for solid electrolytes. The impedance spectra of SS/FG-SPE/SS symmetrical cells at different temperatures are shown in Fig. S13,† and the temperature-dependent ionic conductivities were obtained, as shown in Fig. 5b. The ionic conductivity of FG-SPE was $2.45 \times 10^{-4} \text{ S cm}^{-1}$ at 25 °C, which is extremely significant for practical battery applications. Notably, the inorganic LGPS additive increased the conductivity of PDVC-SPE, as shown in Fig. 5b

and S14,† which was because the nanoparticle additive could inhibit polymer crystallization and increase the free Li⁺ concentration.^{9,13} The ionic conductivities of SPEs based on different LGPS contents from 0%–20 wt% at room temperature were investigated, as shown in Fig. S15.† It was found that the excessive fillers led to a decrease in ionic conductivity, which was attributed to the nanoparticle aggregation, phase separation, and more interfaces in the composite SPE.^{24,25} Fig. S16† displays the Li⁺ transference number of FG-SPE containing a cellulose separator. According to the Bruce–Vincent–Evans equation, the value of t_{Li^+} could be easily confirmed as ~ 0.62 . A high Li⁺ transference number can alleviate the electrode polarization and allow operating a battery under high current density.³³ Moreover, a Li/FG-SPE/Cu cell was assembled to test the coulombic efficiency for Li plating/stripping at the current density of 0.02 mA cm^{-2} . As shown in Fig. S17,† the cell generally exhibited a stable Li plating/stripping behavior despite some initial fluctuation, probably due to the reaction between LGPS or the polymer and Li metal, which indicated that FG-SPE was stable toward Li metal after the formation of a reliable interface.

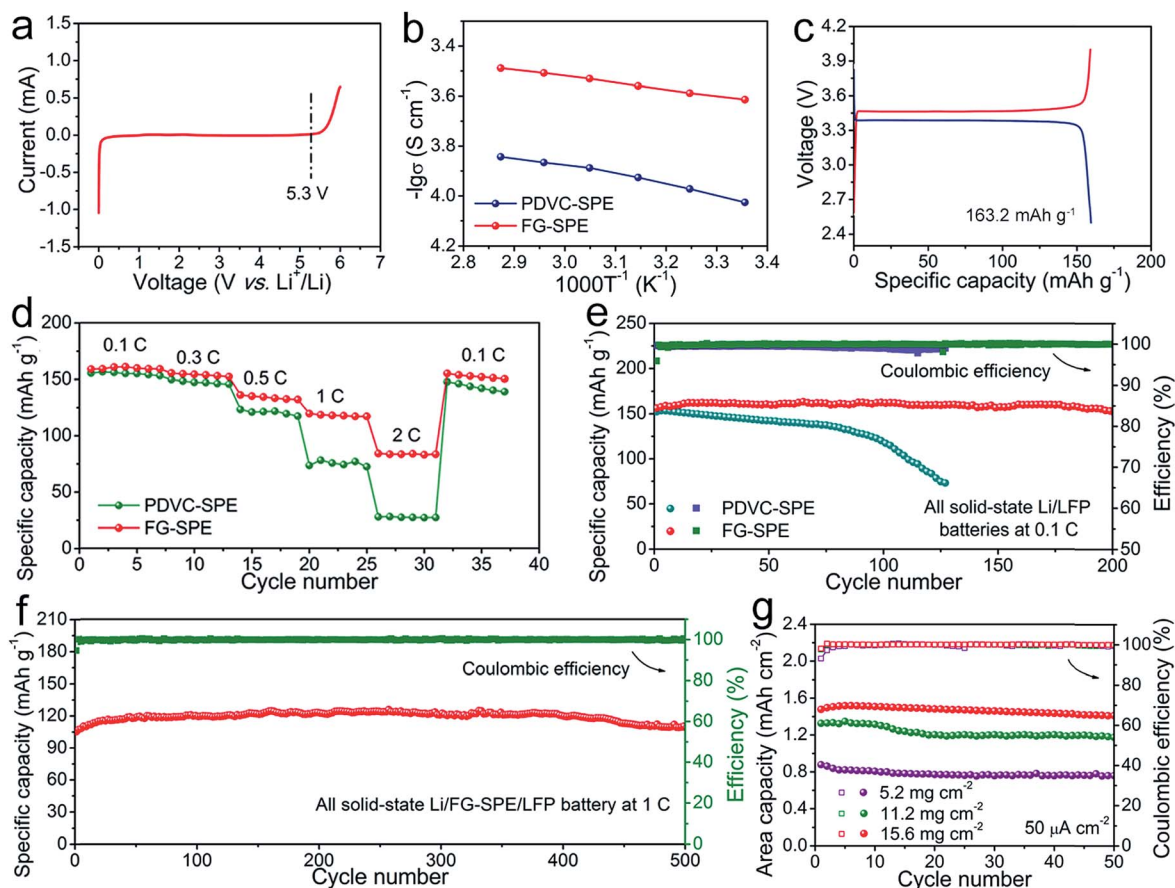


Fig. 5 Electrochemical properties of FG-SPE and the resultant batteries. (a) Linear voltammogram of Li/FG-SPE/SS, showing the electrochemical stability window in the range of 0–5.3 V. (b) Comparison of the temperature-dependent ionic conductivity of PDVC-SPE and FG-SPE. (c) Discharging/charging curves of Li/FG-SPE/LFP battery. (d) Rate performance and (e) cycling performance comparison at a 0.1C rate between Li/PDVC-SPE/LFP and Li/FG-SPE/LFP batteries. (f) Long-term cycling performance of Li/FG-SPE/LFP cell discharging/charging at the current rate of 1C for 500 cycles. (g) Cycling performance of Li/FG-SPE/LFP battery at a high LFP mass loading (11.2 and 15.6 mg cm^{-2}).

The electrochemical performances of FG-SPE-based lithium metal batteries were studied by employing LFP as the cathode. Fig. 5c shows the charge/discharge curves of a Li/FG-SPE/LFP cell at 0.1C rate with the voltage window of 2.5–4.0 V. The battery delivered a high reversible capacity of $\sim 163.2 \text{ mA h g}^{-1}$, which was attributed to the great ionic conductivity of FG-SPE at room temperature and the excellent interfacial compatibility between the polymer electrolyte and electrodes. Fig. 5d depicts a comparison of the rate performances between Li/PDVC-SPE/LFP and Li/FG-SPE/LFP batteries. Although the two cells showed close reversible discharge capacities at low rates, a high capacity could not be achieved in the Li/PDVC-SPE/LFP cell when the current rates were increased to 1C and 2C. In contrast, a high reversible specific capacity of 76.9 mA h g^{-1} could still be obtained even at 2C rate in the Li/FG-SPE/LFP cell (Fig. S18†). A single stiffness property of SPEs can help to resist the dendrite growth but is adverse to a good interface connection, which would severely increase the resistance across the interface and deteriorate the rate capacities. Fig. S19† shows the rate performance of a solid-state battery based on a completely rigid SPE (CR-SPE), similar to the compact ceramic-rich phase of FG-SPE, as an electrolyte. The poor rate properties indicated that the ionic transfer in the resulting cell was difficult to achieve, especially when discharging/charging at high current rates. It was noteworthy that the Li/FG-SPE/LFP battery exhibited excellent cycling performances, as demonstrated in Fig. 5e, and presented almost no decrease in capacity during 200 cycles at the current rate of 0.1C. In contrast, the Li/PDVC-SPE/LFP battery exhibited a slow decay of capacity during early cycling, but a sharp drop after 80 cycles, which was because the accumulated dendrites penetrated the PDVC-SPE. Using the completely rigid SPE as the electrolyte, although the resultant Li/LFP cell displayed a stable cycling process, the battery had much lower specific capacities ($< 112.5 \text{ mA h g}^{-1}$ initially at 0.1C) than the Li/PDVC-SPE/LFP cell, attributed to the poor interface contact (Fig. S20†). The EIS instrument analysis of Li/LFP cells based on PDVC-SPE, CR-SPE, and FG-SPE before and after cycling was further conducted, as shown in Fig. S21a and b.† After cycling, the interfacial resistance of the Li/PDVC-SPE/LiFePO₄ cell showed an obvious increase, demonstrating the deterioration of the electrode/electrolyte interface during continual lithiation/delithiation process. For the Li/CR-SPE/LiFePO₄ cell, it always demonstrated huge interfacial resistance, which was attributed to the hard solid–solid contact and poor interfacial connection; whereas the FG-SPE-based Li symmetric cell always demonstrated a relatively lower resistance, indicating the compatible Li/electrolyte connection and long-term stable contact interface. After 500 cycles at 1C rate, the specific capacity of the Li/FG-SPE/LFP battery could be maintained at $110.5 \text{ mA h g}^{-1}$, demonstrating almost no decay in comparison with the initial capacity (Fig. 5f). Furthermore, we demonstrated the performances of Li/FG-SPE/LFP batteries with high LFP loadings of 11.2 and 15.6 mg cm^{-2} , which delivered areal capacities of $1.25 \text{ mA h cm}^{-2}$ and $1.54 \text{ mA h cm}^{-2}$ at an areal current density of $50 \mu\text{A cm}^{-2}$, respectively, (Fig. 5g), indicating the feasibility of practical all-solid-state battery operation.

Conclusions

In summary, we fabricated an ultrahigh modulus SPE with a functional-gradient-structure by integrating a ceramic-rich phase, acting as a physical barrier to lithium dendrite growth, and a polymer-rich phase, which acted to improve the interface compatibility between the cathode and electrolyte. AFM investigations indicated that the modulus of the ceramic-rich phase was greatly increased to 6.67 GPa from 0.25 GPa, which indicated it was very effective for prohibiting the penetration of Li dendrites. A fabricated all-solid-state battery with the high modulus SPE delivered a high capacity of $163.2 \text{ mA h g}^{-1}$ at current rate of 0.1C at room temperature and the battery's cycle life could be extended to 500 cycles at 1C rate. Importantly, the cathode loading could be up to 15.6 mg cm^{-2} and the areal capacity was thus enhanced to $1.54 \text{ mA h cm}^{-2}$, which paves the way for its application in high-energy all-solid-state Li metal batteries.

Experimental section

Chemicals

Diallyl carbonate (DAC, 99%, Sigma-Aldrich), vinylene carbonate (VC, DodoChem), 2,2'-azobis(2-methylpropionitrile) (AIBN, 98%, Aladdin), lithium bis(trifluoromethanesulfonyl) imide (LiTFSI, DodoChem), Li₁₀GeP₂S₁₂ (LGPS, Kejing MTI), LiFePO₄ powder (Kejing MTI), 1-methyl-2-pyrrolidinone (NMP, 99.5%, Alfa Aesar), and polyvinylidene difluoride (PVDF, Kejing MTI) were all purchased commercially and used without further purification.

In situ preparation of FG-SPEs and PDVC-SPEs in Li/LFP batteries

First, 20 wt% LiTFSI was dissolved in DAC/VC (1/9 weight ratio) mixture to form a homogeneous and transparent solution. Then, the precursor solution of FG-SPE was obtained by adding AIBN and 5 wt% of LGPS nanoparticles. The PDVC-SPE precursor solution was obtained in a similar method as that used for FG-SPE but without the LGPS additive. The whole preparation process was carried out in Ar atmosphere. Before fabricating the SPE-based Li/LFP cells, the LFP cathode needed to be prepared. The LFP powder was mixed with carbon black and polyvinylidene fluoride at a weight ratio of 8 : 1 : 1 with NMP as the solvent to form a homogeneous slurry. The average areal mass loading of LFP was 4.6 mg cm^{-2} . A higher loading of up to 11.2 and 15.6 mg cm^{-2} was utilized. Subsequently, the 2025-type cell was assembled and the prepared precursor solution was incorporated into a cellulose separator. Later, the batteries were kept constantly at 80 °C for 48 h to complete the polymerization of the electrolytes.

Characterizations

The morphologies of the SPEs and cycled Li foils were observed by field emission scanning electron microscopy (SEM, SU8010, Japan) operated at 5.0 kV. Fourier transform infrared (FTIR) spectra were recorded on a Nicolet is50 spectrometer

(ThermoFisher Scientific, America). The Young's modulus of FG-SPE and PDVC-SPE were studied by an AFM instrument (Bruker DIMENSION ICON with a Nanoscope V controller). The mechanical property of the polymer-rich layer was studied by measuring the normal deflection signal change of the cantilever during the tip loading and unloading at the top surface of the FG-SPE sample. Similarly, the modulus of the ceramic-rich layer was characterized by tapping the bottom surface of the FG-SPE sample and then analyzing the recorded force–distance curve. The topographic images were recorded through tapping mode imaging with sharp AFM tips (BRUKER TESP-V2). The force–distance curve was obtained from AFM indentation tests. The parameters of the AFM tips were 40 N m^{-1} and 200 N m^{-1} , corresponding to the modulus ranges of 0.2–2.0 GPa and 1.0–20 GPa, respectively. The maximum indentation force was kept constant at 150 nN for each test. The scan size was $0.5 \times 0.5 \mu\text{m}$.

In situ optical microscopic observations

In situ observations were carried out in the homemade optical cell with a quartz window for observation. PDVC-SPE-covered Li and FG-SPE-covered Li needed to be prepared first. The precursor solutions of PDVC-SPE and FG-SPE were dropped on Li foils, and after polymerization at $80 \text{ }^\circ\text{C}$ for 48 h, the Li foils ($4 \text{ mm} \times 30 \text{ mm}$) were covered with PDVC-SPE and FG-SPE, respectively. Subsequently, bare Li foil, PDVC-SPE-covered Li, and FG-SPE-covered Li were, respectively, employed as working electrodes and immobilized in the optical cells, where bare Li foils were always used as counter electrodes. After injecting the electrolyte, the cells were well-sealed. The assembly of optical cells was performed in an argon-filled glove box with a water and oxygen content of less than 0.1 ppm. An optical microscope with a fitted charge coupled device (CCD) camera was applied to shoot the Li deposition process.

Electrochemical measurements

Symmetrical cells with two identical Li foils were assembled using FG-SPE or PDVC-SPE to study the Li stripping/plating processes. The charge/discharge process was monitored in galvanostatic mode using a CT2001A cell test instrument (Wuhan LAND Electronics Co., Ltd.). A Li/FG-SPE/SS asymmetrical cell was assembled to evaluate the electrochemical stable window of FG-SPE.

The ionic conductivities of FG-SPE and PDVC-SPE were determined *via* an AC technique. The electrolyte was sandwiched between two stainless steel parts. Data were acquired using a CHI660E electrochemical workstation (Shanghai Chenhua Instrument Co., Ltd) with AC voltage amplitude of 10 mV over the frequency range from 0.1 Hz to 1 MHz. The ionic conductivity of the polymer electrolyte was calculated by using the following equation:

$$\sigma = \frac{L}{SR}$$

where L presents the thickness of the polymer electrolyte, S is the contact area between the electrode and electrolyte, and R corresponds to the bulk resistance of the polymer electrode.

Conflicts of interest

There are no conflicts to declare.

Acknowledgements

We acknowledge support from the National Natural Science Foundations of China (grants 51622208, 21703149, 5192500409, and 51872193).

References

- 1 W. Xu, J. Wang, F. Ding, X. Chen, E. Nasybulin, Y. Zhang and J. G. Zhang, *Energy Environ. Sci.*, 2014, **7**, 513–537.
- 2 H. Kim, G. Jeong, Y. U. Kim, J. H. Kim, C. M. Park and H. J. Sohn, *Chem. Soc. Rev.*, 2013, **42**, 9011–9034.
- 3 J. M. Tarascon and M. Armand, *Nature*, 2001, **414**, 359–367.
- 4 R. Zhang, N. W. Li, X. B. Cheng, Y. X. Yin, Q. Zhang and Y. G. Guo, *Adv. Sci.*, 2017, **4**, 1600445.
- 5 K. Zhang, G. H. Lee, M. Park, W. J. Li and Y. M. Kang, *Adv. Energy Mater.*, 2016, **6**, 1600811.
- 6 E. Cha, M. D. Patel, J. Park, J. Hwang, V. Prasad, K. Cho and W. Choi, *Nat. Nanotechnol.*, 2018, **13**, 337–344.
- 7 R. Zhang, X. R. Chen, X. Chen, X. B. Cheng, X.-Q. Zhang, C. Yan and Q. Zhang, *Angew. Chem., Int. Ed.*, 2017, **56**, 7764–7768.
- 8 E. Quartarone and P. Mustarelli, *Chem. Soc. Rev.*, 2011, **40**, 2525–2540.
- 9 L. Fan, S. Wei, S. Li, Q. Li and Y. Lu, *Adv. Energy Mater.*, 2018, **8**, 1702657.
- 10 D. Lin, P. Y. Yuen, Y. Liu, W. Liu, N. Liu, R. H. Dauskardt and Y. Cui, *Adv. Mater.*, 2018, **30**, 1802661.
- 11 R. Khurana, J. L. Schaefer, L. A. Archer and G. W. Coates, *J. Am. Chem. Soc.*, 2014, **136**, 7395–7402.
- 12 Y. Li, X. Chen, A. Dolocan, Z. Cui, S. Xin, L. Xue, H. Xu, K. Park and J. B. Goodenough, *J. Am. Chem. Soc.*, 2018, **140**, 6448–6455.
- 13 C. Zhao, L. Liu, X. Qi, Y. Lu, F. Wu, J. Zhao, Y. Yu, Y. S. Hu and L. Chen, *Adv. Energy Mater.*, 2018, **8**, 1703012.
- 14 S. Zhang, K. Ueno, K. Dokko and M. Watanabe, *Adv. Energy Mater.*, 2015, **5**, 1500117.
- 15 Q. Pan, D. Barbash, D. M. Smith, H. Qi, S. E. Gleeson and C. Y. Li, *Adv. Energy Mater.*, 2017, **7**, 1701231.
- 16 J. Liu, T. Qian, M. Wang, J. Zhou, N. Xu and C. Yan, *Nano Lett.*, 2018, **18**, 4598–4605.
- 17 X.-B. Cheng, R. Zhang, C.-Z. Zhao and Q. Zhang, *Chem. Rev.*, 2017, **117**, 10403–10473.
- 18 F. Wu, Y.-X. Yuan, X.-B. Cheng, Y. Bai, Y. Lia, C. Wu and Q. Zhang, *Energy Storage Mater.*, 2018, **15**, 148–170.
- 19 X. Xu, S. Wang, H. Wang, C. Hu, Y. Jin, J. Liu and H. Yan, *J. Energy Chem.*, 2018, **27**, 513–527.
- 20 X. Wang, W. Zeng, L. Hong, W. Xu, H. Yang, F. Wang, H. Duan, M. Tang and H. Jiang, *Nat. Energy*, 2018, **3**, 227–235.
- 21 M. D. Tikekar, S. Choudhury, Z. Tu and L. A. Archer, *Nat. Energy*, 2016, **1**, 16114–16120.

- 22 B. Wu, S. Wang, J. Lochala, D. Desrochers, B. Liu, W. Zhang, J. Yang and J. Xiao, *Energy Environ. Sci.*, 2018, **11**, 1803–1810.
- 23 Q. Wang, Z. Wen, J. Jin, J. Guo, X. Huang, J. Yanga and C. Chen, *Chem. Commun.*, 2016, **52**, 1637–1640.
- 24 X. Tao, Y. Liu, W. Liu, G. Zhou, J. Zhao, D. Lin, C. Zu, O. Sheng, W. Zhang, H.-W. Lee and Y. Cui, *Nano Lett.*, 2017, **17**, 2967–2972.
- 25 L. Chen, Y. Li, S. P. Li, L. Z. Fan, C. W. Nan and J. B. Goodenough, *Nano Energy*, 2018, **46**, 176–184.
- 26 B. H. Rabin and I. Shiota, *Mater. Res. Soc. Bull.*, 1995, **20**, 14–18.
- 27 G. Bao and L. Wang, *Int. J. Solids Struct.*, 1995, **32**, 2853–2871.
- 28 B. Kieback, A. Neubrand and H. Riedel, *Mater. Sci. Eng., A*, 2003, **362**, 81–105.
- 29 P. G. Bruce and C. A. Vincent, *J. Chem. Soc., Faraday Trans.*, 1993, **89**, 3187–3203.
- 30 S. Inagi, *Polym. J.*, 2015, **48**, 39–44.
- 31 H. Zarrin, S. Farhad, F. Hamdullahpur, V. Chabot, A. Yu, M. Fowler and Z. Chen, *Electrochim. Acta*, 2014, **125**, 117–123.
- 32 Z. Ogumi, T. Abe, S. Nakamura and M. Inaba, *Solid State Ionics*, 1999, **121**, 289–293.
- 33 J. Chai, Z. Liu, J. Ma, J. Wang, X. Liu, H. Liu, J. Zhang, G. Cui and L. Chen, *Adv. Sci.*, 2017, **4**, 1600377.
- 34 J. Zhou, T. Qian, N. Xu, M. Wang, X. Ni, X. Liu, X. Shen and C. Yan, *Adv. Mater.*, 2017, **29**, 1701294.
- 35 C. Wang, K. R. Adair, J. Liang, X. Li, Y. Sun, X. Li, J. Wang, Q. Sun, F. Zhao, X. Lin, R. Li, H. Huang, L. Zhang, R. Yang, S. Lu and X. Sun, *Adv. Funct. Mater.*, 2019, **29**, 1900392.
- 36 Y. Gao, D. Wang, Y. C. Li, Z. Yu, T. E. Mallouk and D. Wang, *Angew. Chem., Int. Ed.*, 2018, **57**, 13608–13612.
- 37 G. Li, Y. Gao, X. He, Q. Huang, S. Chen, S. H. Kim and D. Wang, *Nat. Commun.*, 2017, **8**, 850–859.
- 38 C. Wang, Y. Gong, J. Dai, L. Zhang, H. Xie, G. Pastel, B. Liu, E. Wachsman, H. Wang and L. Hu, *J. Am. Chem. Soc.*, 2017, **139**, 14257–14264.
- 39 C. Wang, L. Zhang, H. Xie, G. Pastel, J. Dai, Y. Gong, B. Liu, E. D. Wachsman and L. Hu, *Nano Energy*, 2018, **50**, 393–400.
- 40 J. Chai, J. Zhang, P. Hu, J. Ma, H. Du, L. Yue, J. Zhao, H. Wen, Z. Liu, G. Cui and L. Chen, *J. Mater. Chem. A*, 2016, **4**, 5191–5197.